Çukurova Üniversitesi Mühendislik Fakültesi Dergisi, 39(1), ss. 119-132, Mart 2024
Cukurova University Journal of the Faculty of Engineering, 39(1), pp. 119-132, March 2024

The Effect of Riblets on the Aerodynamic Performance of NACA 0018 Airfoil

Emre GÜLER[1] ORCID *0000-0001-7337-8678*
Engin PINAR[2] ORCID *0000-0002-7484-8616*
Tahir DURHASAN[*3] ORCID *0000-0001-5212-9170*

[1]Tarsus University, Department of Aerospace Engineering, Tarsus, Türkiye
[2]Çukurova University, Department of Mechanical Engineering, Adana, Türkiye
[3]Adana Alparslan Türkeş Science and Technology University, Department of Aerospace Engineering, Adana, Türkiye

Geliş tarihi: 12.03.2024 Kabul tarihi: 28.03.2024

Atıf şekli/ How to cite: GÜLER, E., PINAR, E., DURHASAN, T., (2024). The Effect of Riblets on the Aerodynamic Performance of NACA 0018 Airfoil. Cukurova University, Journal of the Faculty of Engineering, 39(1), 119-132.

Abstract

In this numerical study, riblets on the airfoil were utilized to enhance the aerodynamic performance of NACA0018 airfoil. Riblets of identical height and base length are strategically placed on the suction surface of the airfoil with varying spacing ratios along the flow direction (x) and chord length (c), specifically x/c = 0.3 and 0.7. Four distinct riblet airfoil models are subjected to computational fluid dynamics (CFD) analysis within an angle of attack range from 0° to 21° at a Reynolds number of $Re=1\times10^5$. The obtained results are systematically compared with the performance of the plain airfoil. Numerical analyses reveal the significant influence of the spacing ratio on flow control and the overall aerodynamic performance of the airfoil, establishing a direct relationship with riblet spacing. The presence of riblet structures is observed to increase the lift coefficient, concurrently delaying the stall angle up to 19°. Notably, the ribbed structures effectively mitigate the interaction between the laminar separation bubble and trailing edge separation, leading to a reduction in turbulent kinetic energy values.

Keywords: Riblet, Computational fluid dynamics, Flow control, Aerodynamic performance of airfoil

Yivlerin NACA 0018 Kanat Profilinin Aerodinamik Performansı Üzerine Etkisi

Öz

Bu sayısal çalışmada NACA 0018 kanat profilinin aerodinamik performansını arttırmak için yivli yapılar kullanılmıştır. Aynı yüksekliğe ve taban uzunluğuna sahip olan yivler, akış yönü doğrultusunun (x) veter uzunluğuna (c) oranı, x/c = 0,3 ve 0,7 arası boyunca kanat emme yüzeyine farklı boşluk oranları ile yerleştirilmişlerdir. Dört farklı yivli kanat modeli hücum açısının 0^o ile 21^o arasında ve Reynolds sayısının $Re=1\times10^5$ değerinde hesaplamalı akışkanlar dinamiği (HAD) ile analiz edilmiştir. Yivli yapıların etkisini

[*]Sorumlu yazar (Corresponding Author): Tahir DURHASAN, *tdurhasan@atu.edu.tr*

göstermek için elde edilen sonuçlar yalın kanat modeli ile kıyaslamalı olarak sunulmuştur. Sayısal çözümlemelerden elde edilen veriler yiv boşluk oranının akış kontrolü üzerinde etkili olduğunu ve kanat aerodinamik performansının yiv boşluk oranı ilişkili olduğunu ortaya koymuştur. Yivli kanat modelinin taşıma katsayısını artırdığını ve tutunma kaybı açısını 19°'e kadar ötelediği gözlemlenmiştir. Ayrıca yivli yapıların laminer ayrılma kabarcığının ve firar kenarı yarılması etkileşimini bastırdığını böylelikle türbülans kinetik enerji değerlerini azalttığı gözlemlenmiştir.

Anahtar Kelimeler: Yivli yüzey, Hesaplamalı akışkanlar dinamiği, Akış kontrolü, Kanat aerodinamik performans

1. INTRODUCTION

The interest in studies on the aerodynamic performance of airfoils has increased due to the increasing use of unmanned aerial vehicles (UAVs) and micro aerial vehicles (MAVs) in both military and civilian areas.

Since flow around the airfoils directly affects aerodynamic performance, it is significant to examine flow structures. Flow types around airfoils can be classified depending on the Reynolds (*Re*) number. If the flow has a Reynolds number less than 5×10^5, it is referred to as low Reynolds number flow. Low Reynolds number flow conditions are common in engineering applications (such as micro-drones and small-scale wind turbines) and in nature (such as birds and insects). The most basic characteristic of low Reynolds number flows is that the laminar boundary layer, which separates from the airfoil due to strong pressure gradients caused by viscous effects, transition laminar to turbulence and reattach to the surface again, forming a laminar separation bubble. The laminar separation bubble causes structural damage through negative effects, such as decrease in lift and increase in drag, as well as mechanical vibration. To control these effects, control of the flow structure around the airfoil has become one of the priority topics for researchers.

One of the mechanisms used to reduce the drag force is to add a roughness element to the airfoil. These surfaces create small vortices, causing the momentum of the flow to increase. Flow separation may be delayed due to an increase in momentum. By making geometrical changes on the surfaces of different airfoils, a general increase in aerodynamic performance has been achieved by delaying the stall. Huber et. al. [1] experimentally investigated the effect of roughness on the Wortmann FX-63-137 airfoil using wires of different diameter sizes, at angle of attack (α) -16° to 24° and Reynolds number, $Re=1\times10^5$. According to their findings, they revealed that knowing the boundary layer thickness should be the first step for a critical roughness height, and that the change in wire diameter does not increase the aerodynamic performance of the wing in direct proportion. After a certain diameter, this positive effect may reverse due to increase in diameter. They also showed that the stall was prevented depending on the placement of the wire on the wing. Gopalarathnam et. al. [2] conducted both experimental and numerical studies for three different airfoils, SA7024, SA7025, and SA7026. The use of the ramp configuration with the help of trips in different positions on the airfoil's boundary layer was examined in the Reynolds number range of $1\times10^5 < Re < 3\times10^5$. Even though their findings effectively reduce the drag and increase the lift force, they stated that the need for further studies is required for low Reynolds number airfoils. In the study conducted by Sareen et. al. [3], they aimed to reduce the drag force for different flow regimes and thus, control the flow structure with four different V-shaped riblet structures on the DU 96-W-180 airfoil used for wind turbines. Among the riblet height configurations of 44, 62, 100 and 150 μm used, it was observed that the drag coefficient decreased for the riblet with a height of 62 μm. In addition to wing profiles, the effect of riblets were investigated on different basic geometries, including cavities, cylinders, and others. Lee et. al. [4] performed an experimental study by coating a circular cylinder with a completely riblet film. The height of the V-shaped micro-sized riblets was chosen as 180 μm and the gap between them was 300 μm, and they were placed along the entire surface of the cylinder and

analyzed for different Re numbers. The findings showed that although the drag coefficient decreased by 7.6% at Re=3.6×10^3, it was increased by approximately 4.2% at Re=3.6×10^4. Vilkinis et. al. [5] experimentally examined the effect of triangular riblets added into cavity. They found that as a result of decreasing the distance between the riblets placed inside the cavities, the pressure loss increased, and as the size inside the cavity decreased, the interaction between the main flow and the flow in the subcavities decreased, resulting in a decrease in pressure losses. Moreover, we have observed that the use of riblet surface is an effective flow control method for different wing profiles, as it is also effective on wing aerodynamics. Zhang et. al. [6] applied the large eddy simulation to reveal the effect of V-type isosceles-shaped riblets placed on the Eppler E374 airfoil for a constant angle of attack (α). The riblets on the airfoil were placed along the chord length (c) ratio between x/c=0.3 and x/c=0.99, and also the effects of adding a trip on the wing at x/c=0.13 were investigated on the aerodynamic performance of the airfoil. The findings showed that the used methods were effective in increasing the lift coefficient, decreasing the drag coefficient, and reducing the effectiveness of Reynolds stress values and vortex structures. However, one of the important parameters affecting vortex shedding in different geometric structures is the angle of attack [7].

NACA airfoils have been the research subject of many studies due to their widespread use in practice [8-13]. Lee et. al. [14] experimentally examined the effect of the micro-riblet film placed on the suction side of the NACA0012 airfoil. In comparison to the base airfoil, the use of V-shaped riblet grooves resulted in a 6.6% reduction in drag force for the value of Re=1.54×10^4, whereas it increased by 9.8% at Re=4.62×10^4. Wu et. al. [15] numerically examined the riblet effect on the NACA0012 airfoil in low Re number flow regimes. The riblets are placed on the airfoil in two different configurations: the middle part, where the chord (c) length ratio ranges from x/c=0.3 to x/c=0.7, and the trailing edge section, designated with ratios ranging from x/c=0.5 to 0.9. It was observed that the drag coefficient was reduced by 9.65% for the most effective riblet height of 0.1 mm. Tiainen et. al. [16] experimentally studied the NACA0024 airfoil by creating 30° angle trapezoidal riblet structures with height (h) and spacing (s) of h=0.149 mm and s=0.298 mm, in the Reynolds number range of $8.3\times10^4<Re<2.48\times10^5$. The riblets used in the experiments were placed on the airfoil at the position of the chord length ratio between x/c=0.65 and x/c=0.9, and their quantitative effects on the flow were demonstrated using the Particle Image Velocimetry (PIV) method. According to the findings of the study, a decrease of up to 6.8% in drag force and a decrease of up to 80% in Reynolds stress values were determined. They also revealed that the airfoil with riblets could increase the power coefficient of a horizontal axis wind turbine by 10.9%. Yang et. al. [17] numerically investigated V-type riblet structures on the NACA4412 airfoil for different angles of attack and different riblet lengths in the low Re number flow regime. They determined that the most effective riblet length was 0.8c, and in this case, there was a 17.46% increase in lift force and a 15.04% decrease in drag force. In addition to employing riblets, various studies in the literature explore the application flaps added to the trailing edge of the airfoil for flow control. For instance, Meena et. al. [18] examined the effects on wing aerodynamics by adding Gurney flap on four different airfoils, namely NACA0000 (flat plate), 0006, 0012, and 0018, for low Reynolds number flow regime. In the numerical study conducted for varying angles of attack of the airfoil and different heights of the Gurney flap added to the trailing edge, an almost twofold increase in the lift-to-drag ratio was observed. They determined that the maximum lift-drag ratio was obtained at the Gurney flap height (h) value of h/x = 0.1 for all airfoil profiles. Göv et. al. [19] proposed a flexible airfoil that can be changed during flight instead of making additions to the airfoil. Numerical analyzes conducted within the range of *Re*=5×10^4 and for angles of attack $0°\leq\alpha\leq23°$ indicated that the utilization of modified airfoil shapes in the NACA4412, yielded effective aerodynamic results especially during takeoff and climb phases, delaying stall occurrence at increased angles of attack. The studies mentioned so far have been

carried out by using fixed additions on the airfoil to control the flow structure on the airfoil. Additionally, studies have been conducted on delaying the stall angle in NACA airfoils using different methods such as using flexible[10,20] or flapping [21].

Despite the application of various active or passive control methods, there is a need to investigate and diversify alternative control methods that can be applied across different angles of attack and flow velocities on airfoils. In this study, our aim is to increase the lift coefficient by introducing a rough structure created by placing different riblet structures on the NACA0018 airfoil, and to delay stall for high angles of attack by shifting the boundary layer separation point. Within the scope of this numerical study, the flow structures and aerodynamic coefficients around 4 different controlled airfoils (M1, M2, M3 and M4) are investigated and the results obtained are presented in comparison with the plain airfoil (M0). The position of the riblets on the airfoil is tested at different angles of attack ($0° \leq \alpha \leq 21°$) by varying the ratio of the flow axis (x) and chord length (c) between x/c=0.3 and 0.7. The obtained results showed that the use of riblet structures on the airfoil is an effective method on flow control and it positively affects the aerodynamic performance of the airfoil by increasing the lift-drag ratio and stall angle.

2. MATERIALS AND METHODS

In this section, the numerical simulation domain, the geometry of the airfoil, mesh information, riblet shapes, locations and dimensions are explained in detail with the help of the presented figures. In this study, two-dimensional numerical analyzes were carried out at a value of 1×10^5 of Reynolds number ($Re = \rho\ U_\infty\ c\ /\ \mu$) using the ANSYS Fluent, computational fluid dynamics (CFD) program. In the dimensionless Reynolds number formula, ρ is the density of the fluid, U_∞ is the free flow velocity, c is the airfoil chord length and μ is the dynamic viscosity of the fluid.

The aerodynamic performances of the airfoils were examined with the lift coefficient (C_L) (Equation 1), drag coefficient (C_D) (Equation 2) and pressure coefficients (C_P) (Equation 3) obtained for different angles of attack.

$$C_L = \frac{F_L}{\frac{1}{2}\rho U_\infty^2 A} \tag{1}$$

$$C_D = \frac{F_D}{\frac{1}{2}\rho U_\infty^2 A} \tag{2}$$

$$C_P = \frac{P - P_\infty}{\frac{1}{2}\rho {U_\infty}^2} \tag{3}$$

In the formulas given above, F_L is the lift force, F_D is the drag force, P is the static pressure at the point measured on the airfoil, P_∞ is the static pressure of the free stream, ρ is the fluid density, V_∞ is the free flow speed and A is the airfoil reference area.

2.1. Model and Mesh Structure

Within the scope of the study, in order to reveal the effect of riblet, numerical analyzes were first carried out for the NACA 0018 airfoil that does not have a control element. The chord length (c) of the airfoil was chosen as 200 mm. The flow field is shown in Figure 1 and the coordinate system is placed on the trailing edge of the airfoil. To prevent possible deterioration of the structure around the airfoil due to wall effects, the flow field was extended by 12.5c on the y-axis and 25c on the x-axis. In particular, a C-type mesh structure was employed to enhance the resolution of the boundary layer on the airfoil. The mesh structure was created in the ICEM CFD program. The mesh structure around the NACA 0018 airfoil is shown in Figure 2. A total of 500,000 mesh cells were created, and the upper and lower surfaces of the airfoil were divided into sections with 350 and 310 nodal points, respectively. Mesh quality is given in Table 1.

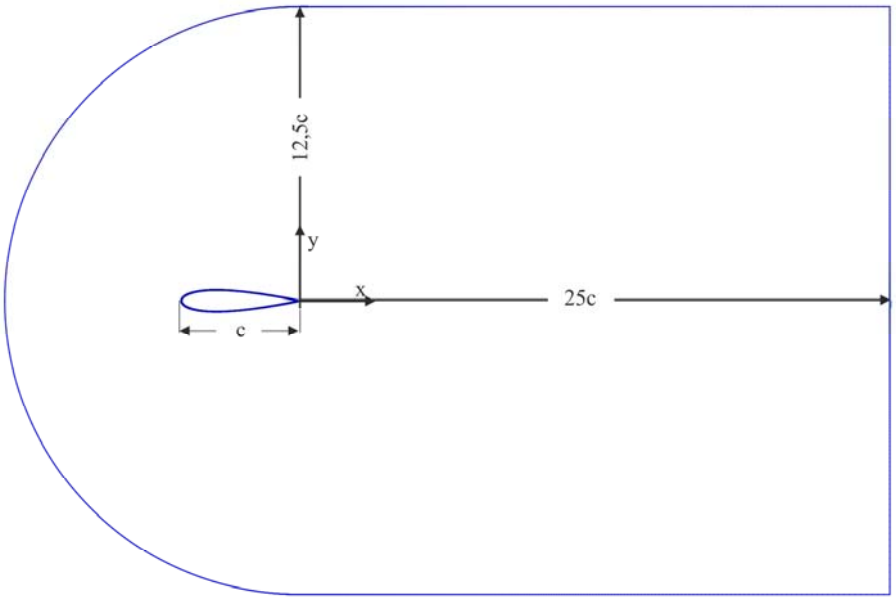

Figure 1. Schematic view of flow domain

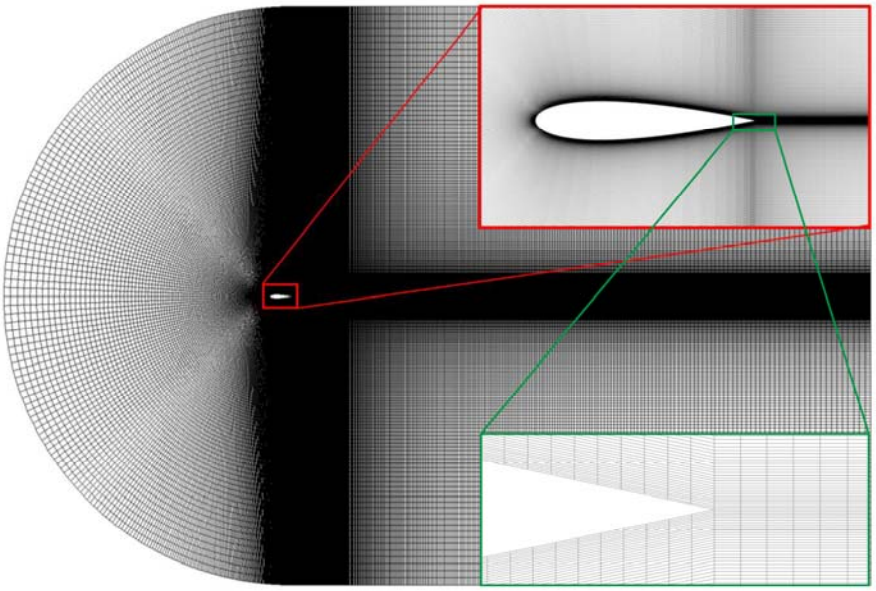

Figure 2. Mesh Structure around airfoil

As seen in Figure 1, the mesh structure has been developed to achieve a more precise solution at the boundary layer, with increased density as it approaches the airfoil surface. The mesh structure was designed with a y+ value less than 1, as depicted in Figure 3, and the first layer thickness on the airfoil was determined to be 2.6×10^{-5} m.

Table 1. Mesh quality values

	Minimum	Maximum	Average	Standard deviation	Fluent user manuel
Skewness quality	1.3×10^{-10}	0.13	0.024	0.0390	Max. Skewness<0.25, Excellent
Orthogonal quality	0.83	1	0.997	0.00555	0.7<Min. Orthogonal Quality<0.95, Very Good

We aimed to increase the aerodynamic performance of the NACA 0018 airfoil by using the riblet control element. The riblet parameters are shown in Figure 2 in detail. Figure 4 shows the riblet height (h), riblet base length (w), and the gap (s) between two riblet base corners. A study was conducted by Wu et. al. [15] on the NACA 0012 airfoil to reduce drag by means of triangular riblets placed on the suction surface. In their study, cavity surfaces were created on the airfoil, cavity dimensions were determined as h = s = w, and four different values of the gap parameter were examined numerically. Unlike the previous study, in this investigation, the riblets were strategically positioned to induce surface roughness on the suction side of the airfoil. The riblet parameters were chosen as height, position, number of riblets and distance between two riblets. Four different airfoil models were created depending on these parameters, and the dimensionless values of the parameters according to the chord length of the airfoil are given in Table 2.

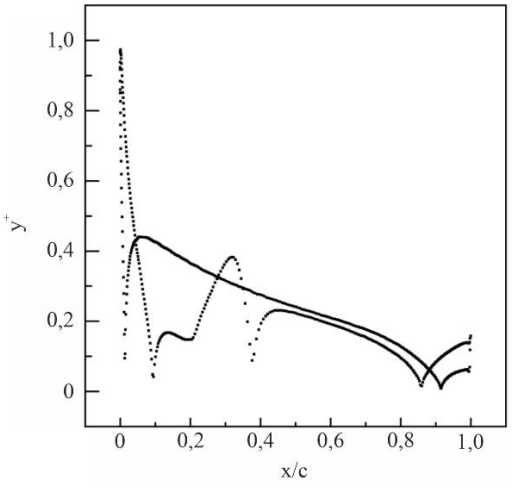

Figure 1. Distribution of y+ over airfoil

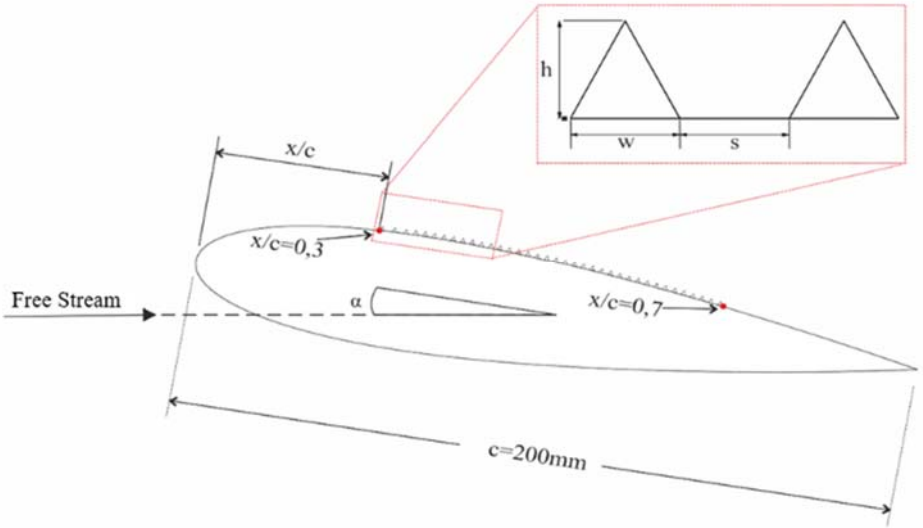

Figure 2. Representation of riblets on the airfoil

The airfoil models employed in the study are denoted as M0, M1, M2, M3, and M4. The M0 model represents the plain NACA 0018 airfoil and serves as a reference to elucidate the impact of the riblet. In all models, the riblets are placed on the suction surface of the airfoil and at the 0.3<x/c< 0.7 position of the airfoil as illustrated in Figure 4 and have the same height (h) and width (w). From the M1 model to the M4 model, the size of riblet region on the airfoil was increased by gradually reducing the gap between the riblet. The riblet gap ratios for M1, M2, M3 and M4 models are s/c=0.1, 0.01, 0.005 and 0, respectively. For the M4 model, the riblet gap ratio s/c=0 means that the airfoil is completely covered with riblets with a range of 0.3<x/<0.7 and there is no gap between the riblets.

Table 1. Information of riblet models: location (x/c), height (h/c), width (w/c), and gap ratio (s/c)

	x/c	h/c	w/c	s/c
M0	-	-	-	-
M1	0.3<x/c<0.7	0.005	0.005	0.1
M2	0.3<x/c<0.7	0.005	0.005	0.01
M3	0.3<x/c<0.7	0.005	0.005	0.005
M4	0.3<x/c<0.7	0.005	0.005	0

Numerical analyzes for all models were carried out at Reynolds number Re=1×10^5 and angle of attack range from α=0° to α=21°. The detailed mesh structures of both the controlled NACA 0018 airfoil with riblets are provided in Figure 5. The total number of cells is approximately 500,000. Similar to the y$^+$ value specified in the plain model; the design criterion for all controlled airfoils is y$^+$<1.

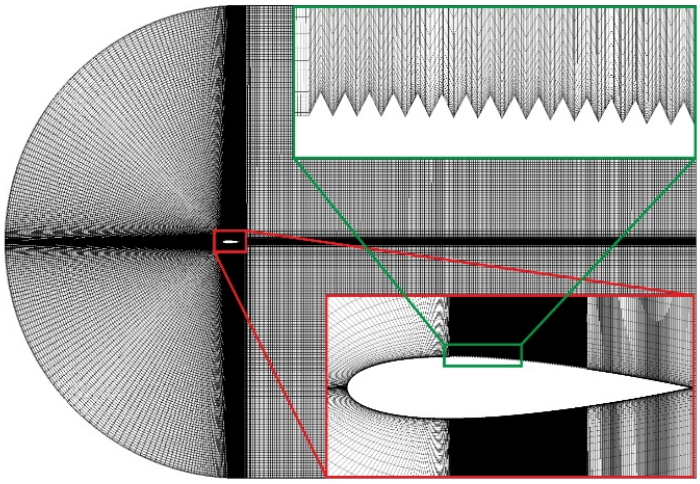

Figure 3. Mesh structure around riblet airfoil

The continuity (Equation 4), momentum (Equation 5) and energy (Equation 6) equations were analyzed with the ANSYS Fluent. In the equations, p represents static pressure, $\bar{\tau}$ is the stress tensor, and $\rho\vec{g}$ is the gravitational force. In the energy equation, k_{eff} denotes the effective conductivity and $\vec{J}_j$ denotes the diffusion resultant. The right-hand side of Equation 6 represents energy transfer due to conduction, diffusion, and viscous dissipation, respectively. Additionally, S_h consists of chemical reaction heat and other volumetric heat sources.

$$\frac{\partial \rho}{\partial t} + \nabla \cdot (\rho \vec{v}) = 0 \tag{4}$$

$$\frac{\partial}{\partial t}(\rho \vec{v}) + \nabla \cdot (\rho \vec{v} \vec{v}) = -\nabla p + \nabla \cdot (\bar{\bar{\tau}}) + \rho \vec{g} + \vec{F} \tag{5}$$

$$\frac{\partial}{\partial t}(\rho E) + \nabla \cdot (\vec{v}(\rho E + p) = \nabla \cdot \left(k_{eff} \nabla T - \sum_j h_j \vec{J}_j + (\tau_{eff} \cdot \vec{v}) \right) + S_h \quad (6)$$

Numerical analyzes were carried out with a two-dimensional, density-based, implicit formulation and k-k_L-ω turbulence transition model. The transition model introduced by Walters et. al. [22] is used to predict boundary layer development and calculate the onset of transition. This model is useful for modeling the transition of the boundary layer from the laminar regime to the turbulent regime, and studies in the literature clearly demonstrate the effectiveness of the model [23-27].

The k-kL-ω transition model consists of a three-equation of eddy-viscosity type (Equations 7, 8, 9). In this model, kT refers to turbulent kinetic energy, kL refers to laminar kinetic energy, and ω refers to the specific dissipation rate. All details about transport equations and constants can be found in the study of [22].

$$\frac{Dk_T}{Dt} = P_{k_T} + R_{BP} + R_{NAT} - \omega k_T - D_T + \frac{\partial}{\partial x_j}\left[\left(v + \frac{\alpha_T}{\sigma_k}\right)\frac{\partial k_T}{\partial x_j}\right] \quad (7)$$

$$\frac{Dk_L}{Dt} = P_{k_L} + R_{BP} + R_{NAT} - D_L + \frac{\partial}{\partial x_j}\left[v\frac{\partial k_L}{\partial x_j}\right] \quad (8)$$

$$\frac{D\omega}{Dt} = C_{\omega L}\frac{\omega}{k_T}P_{k_T} + \left(\frac{C_{\omega R}}{f_W} - 1\right)\frac{\omega}{k_T}(R_{BP} + R_{NAT}) - C_{\omega 2}\omega^2 + C_{\omega 3} f_\omega \alpha_T f_W^2 \frac{\sqrt{k_T}}{d^3} + \frac{\partial}{\partial x_j}\left[\left(v + \frac{\alpha_T}{\sigma_\omega}\right)\frac{\partial \omega}{\partial x_j}\right] \quad (9)$$

All analyzes were performed based on steady-state solutions, using the coupled-implicit algorithm scheme with a density-based solver. The least square cell-based method was used for the gradient and the second order discretization method was applied for all other parameters in the spatial discretization. The airfoil surface was accepted as the non-slip wall condition and the flow field was solved with the pressure far field condition for a hydraulic diameter of 0.196 m with 5% turbulence intensity. The outputs of the parameters were adjusted according to 10^{-8} absolute convergence criterion.

To validate the accuracy of the numerical solution model employed in this study, we carried out the study conducted by Yang et. al. [17] on the NACA 4412 with riblets for Re=1x10^5 and angles of attack (α) of 6° and 8°. The C_L values obtained from numerical solutions are presented comparatively in Table 2. The findings obtained revealed the accuracy of the solution models with small margins of error.

Table 2. Comparison of lift coefficient for validation of numerical studies

Angle of attack	Yang et. al. (2021)	Our results	Error
6°	0.91	0.90	-%1.1
8°	1.09	1.095	+%0.45

3. RESULTS AND DISCUSSIONS

In Figure 4, the lift (C_L) and the lift-drag ratios (C_L/C_D) are given for angles of attack of α=0°, 4°, 8°, 10°, 13°, 15°, 17°, 19° and 21°, respectively. It is evident from this figure that the impact of the control element is negligible up to the angle of attack of α=13°. For cases M1 and M4, the results are approximately similar as those obtained from the M0 model (airfoil with no control element) while the M2 and M3 models have a negative lift coefficient at α=0° due to the higher pressure on the upper (suction) surface of the airfoil. Upon examination of the results obtained from the M1, M2, M3 and M4 models at angle of attack of α=4°,

it was observed that they showed lower lifting performance in comparison with the M0 model. In addition, the M2 model has the lowest lift coefficient value compared to the M0 model for the same angle of attack and about 90% decrease in aerodynamic performance is observed. The results obtained from all models exhibit a similar trend at the angles of attack of α=8° and α=10°, the lift coefficient value of the M0 model at α=13° is slightly lower than other models where the control element is used. The lift coefficient value of the M3 and M4 models increased by 9% compared to the M0 model at α=13°. It is clearly seen in Figure 4(a) that α=13° is the stall angle of M0 model. On the other hand, it can be inferred that on airfoils where the control element is used, the stall angle is delayed. The stall angle is determined as α=15° for the M1 model, while for the M2 and M3 models, it is determined as α=17°. The fact remains that the stall angle for the M4 model has shifted to an angle of attack of α=19°. For the M4 model, the stall angle is delayed by 6°, and an improvement of nearly 34% in the lift coefficient is determined at the angle of attack of α = 13° compared to the plain airfoil profile.

The ratio of lift-drag coefficients of the models using the control element shown in Figure 4 (b) are lower than the M0 model for α≤10°. It is determined that the lift-drag ratio of the M2 model is reduced by 95%. While the lift-drag ratio has approximately the same value for angles of attack of α=8° and 10° in all models using a control element, an increase in performance after α=13° is observed by delaying the stall in the models other than M0. For the M4 model, the maximum lift-to-drag ratio is achieved at α=15°, exhibiting a remarkable increase of 272% compared to the M0 model.

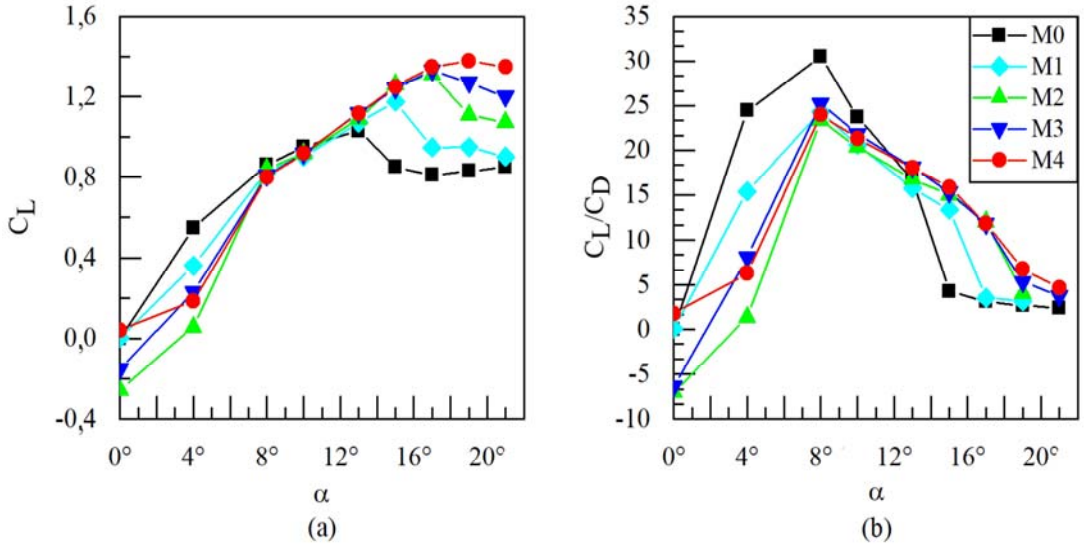

Figure 4. a) Variation of lift coefficient with the angles of attack, b) Variation of lift to drag ratios with the angles of attack

The streamline topologies are presented in Figure 7 for α= 0°, 4°, 8°, and in Figure 6 for α= 13°, 17°, 21° to examine the flow structure around the models. For the M0 model, it is observed that the trailing edge separation, indicated by the symbol F2 in Figure 7, occurs when the angle of attack is α= 0°. It is observed that at α= 4°, in addition to the separation of the trailing edge, a laminar separation bubble (denoted by the symbol F1 in the figure) is formed and with increasing angles of attack, the

laminar separation bubble moved forward to the leading edge. It is discerned that at α = 13°, the separation of the trailing edge moves towards the leading edge, creating a much wider circulating flow region on the airfoil suction surface. At post-stall angles of attack (α=17° and α=21°), the trailing edge separation shifts towards the leading edge, coupled with the presence of a laminar separation bubble, leading to the formation of a continuous circulating flow region (indicated by the symbol F3 in the figure) that spans the airfoil suction surface. It is observed that airfoil models using riblet structures as control elements negatively affect the flow structure at low angles of attack. The fluctuations in the flow structure at the trailing edge are notable at angles of attack α=0° and α=4°, particularly for the M1 and M2 models with a higher gap ratio between riblet structures. Conversely, a more distinct circulating flow region is observed for the M3 and M4 models, where the gap ratio between riblet structures is lower, compared to the clean model. These alterations in the flow structures around the riblet models elucidate the reasons behind the lower lift coefficients compared to the clean model. At an increased angle of attack (α=8°), a laminar separation bubble (F1) forms near the leading edge in all models, terminating at x/c=0.3. Moreover, it is noted that the bubble length in the M2 and M4 models is smaller than in the other models. At angle of attack of α=13°, the advancement of trailing edge separation towards the leading edge is stopped by the help of riblets, occurring approximately at the chord length ratio x/c=0.7. Consequently, in contrast to the M0 model, an increase in lift coefficient is observed, preventing stall. At α=17°, laminar separation and trailing edge separation coalesce to form a broad circulation region post-stall for the M1 model. In the M2, M3, and M4 models, while the circulating flow region resulting from trailing edge separation expands, its merging with the laminar separation bubble is prevented. This unequivocally demonstrates the efficacy of the riblet gap ratio as a parameter influencing both aerodynamic forces and flow structure. The streamlines obtained for all models at an angle of attack α=21° delineate the flow structure after stall. While a unified region is formed for M0 and M1 models by the circulation region, transitioning from the M2 model to the M4 model reveals an attempt by the laminar separation bubble and trailing edge separations to maintain distinct structures within the formed circulating flow region on the airfoil suction surface. Consequently, a more flattened circulating flow region is observed, particularly in the riblet structures region of the M4 model. This observation aligns with force coefficient analysis, as depicted in Figure 6, where the M4 model exhibits the highest C_L values.

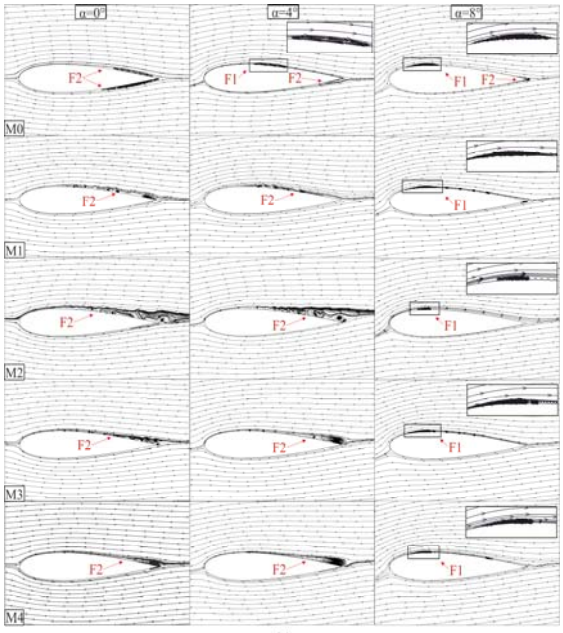

Figure 5. Streamline topologies for different airfoil at angles of attack of α= 0°, 4° and 8°

In Figure 9 and 10, velocity contours in the flow direction around different models are presented for various angles of attack (α = 0°, 4°, 8° in Figure 9, and α = 13°, 17°, 21° in Figure 10). The legend below the velocity contours indicates that red regions signify acceleration resulting from an increase in the angle of attack, while blue regions represent flow separations and bubble formation.

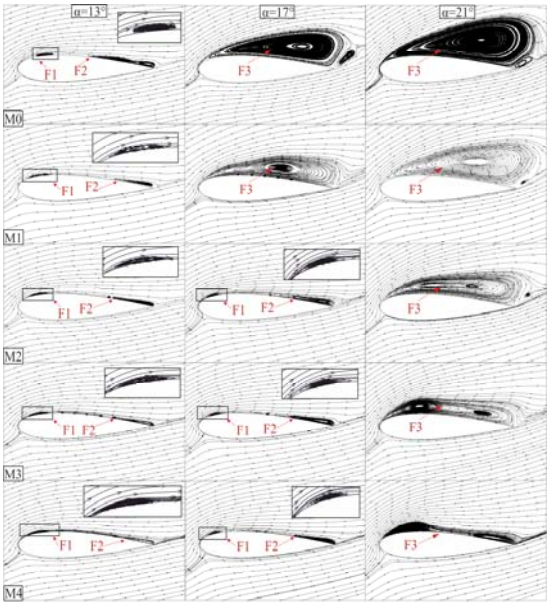

Figure 6. Streamline topologies for different airfoil at angles of attack of α= 13°, 17° and 21°

The contours are drawn with a constant increase in u/U_∞ from low (blue color) to high velocity (red color), maintained at 0.2. As evident from the figure, the velocity increases at the leading edge of the suction surface from α=0° to α=13° before stall angles. Beyond the stall angles, the velocities on the airfoil suction surface decrease with increasing angle of attack. For the M0 airfoil model without a control element, the density of the negative velocity region on the airfoil suction surface significantly increases at α = 17° and 21° due to stall, leading to the circulating flow region mentioned in Figure 6. Additionally, owing to the greater negative velocity values on the airfoil suction surface at high angles, a decrease in pressure difference between the upper and lower regions of the airfoil is observed. In other words, a substantial stall is noted after α=13°. It is observed that the stall angle is effectively increased for all controlled models except the M0 model. Despite an increase in the angle of attack, especially as the distance between the riblets on the airfoil decreases, the negative velocity region on the airfoil is suppressed. The lifting force of the airfoil partially increases up to α=17° for the M1 model and up to α=21° for the M2 and M3 models.

In Figure 11, the variation of the pressure coefficient (C_P) along the chord length is depicted for all models at different angles of attack. The negative values of the pressure coefficient are employed by multiplying the results by -1 to create these graphs. Consequently, positive values above the horizontal axis signify pressure coefficients on the suction (top) surface, while negative values below the horizontal axis indicate pressure coefficients on the pressure (bottom) surface of the airfoil. At low angles of attack, observable fluctuations in both positive and negative pressure coefficients in regions where the control element is utilized suggest the formation of small circulating flow regions. These structures introduce instabilities in the flow, consequently impacting the lift coefficient adversely. Despite a decrease in pressure coefficient fluctuations with an increase in angle of attack, wider gap ratios between riblets persist for the M1 and M2 models at all angles of attack. The peak observed in the positive pressure coefficient distribution for the M0 model at α=4° and chord length ratio x/c=0.5 represents the laminar separation bubble. This peak shifts to lower chord ratio values with increasing angle of attack. In controlled airfoil models, this peak formation is observed at α=8°, aligning with the streamlines. Additionally, at angle of attack α=8°, the re-attachment of the separated boundary layer in the M0 model occurs at x/c=0.38, while for all other models, the re-attachment occurs at x/c = 0.3. This indicates that the groove at x/c=0.3 induces early turbulence transition in the boundary layer, promoting its adherence to the surface. The applied control method's effect is prominently visible at angles of attack (α≥13°) after stall case for M0. At these angles, a more gradual separation occurs instead of a sharp one, and the riblets produce the highest $-C_p$ values. This effect is evident in both the force coefficients graph and the streamline topology. For all controlled models (M0, M1, M2, and M3), at angles of attack α=15°, α=17°, α=19°, and α=21°, respectively, there is a decrease in the highest C_P values due to the combination of laminar separation bubble and trailing edge separation.

When comparing the M0 and M3 airfoil models at α=13°, the maximum reduction in laminar separation bubble length is approximately 30%.

Notably, the formation of the circulating flow region is prevented for the airfoil model M4 due to the zero-gap ratio of the riblets (s/c = 0)

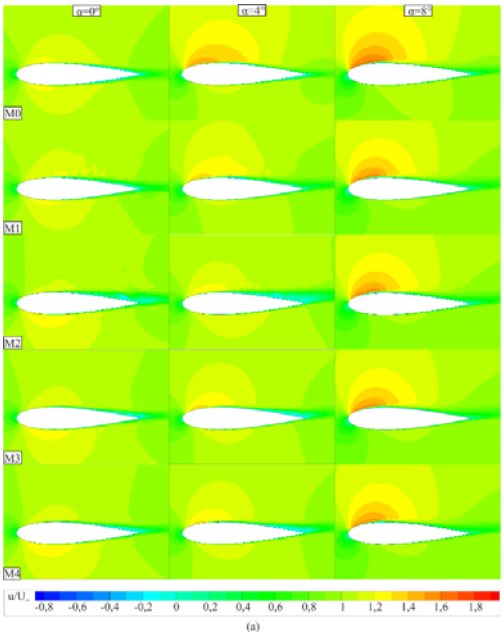

Figure 7. Streamwise velocity contours at angles of attack of α= 0°, 4° and 8°

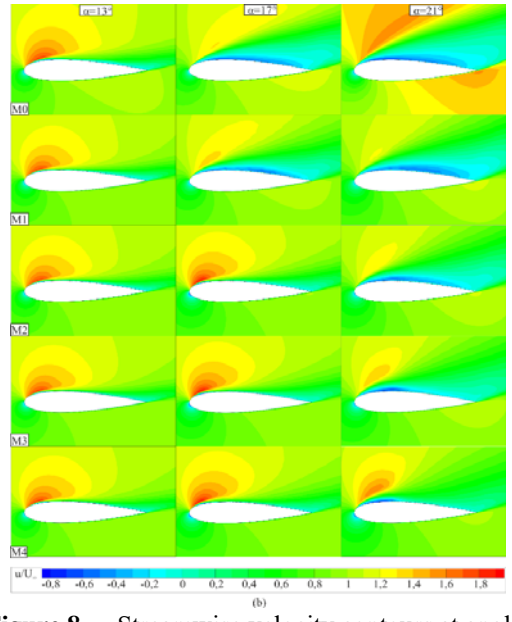

Figure 8. Streamwise velocity contours at angles of attack of α= 13°, 17° and 21°

To elucidate the impact of riblets on the airfoil's turbulent flow structure, Figure 12 displays the distributions of turbulent kinetic energy (TKE) obtained at angle of attack values of α=13°, α=17°, and α=21°. To facilitate the comparison for all models, the increment value in the TKE contours is kept constant as 0.05. At α=13°, the M0 model, lacking a control element, exhibits the highest TKE value. Notably, in all models employing the control element, TKE values are lower, attributable to the constraint imposed by riblets on laminar separation bubble and trailing edge separation. At α=17°, the TKE contours extend over a wide flow area due to the extensive circulation region on the M0 and M1 models. At α=21°, the turbulence kinetic energy region expands for both models with and without a control element. The diminishing extent of high-energy TKE contour regions in models with the control element underscores the efficacy of the applied control method in delaying stall at high angles of attack (α=13° and 17°). Furthermore, these findings suggest that beyond improving aerodynamic performance, the control method has the potential to mitigate adverse effects such as vibrations by reducing the turbulent zone around the airfoil.

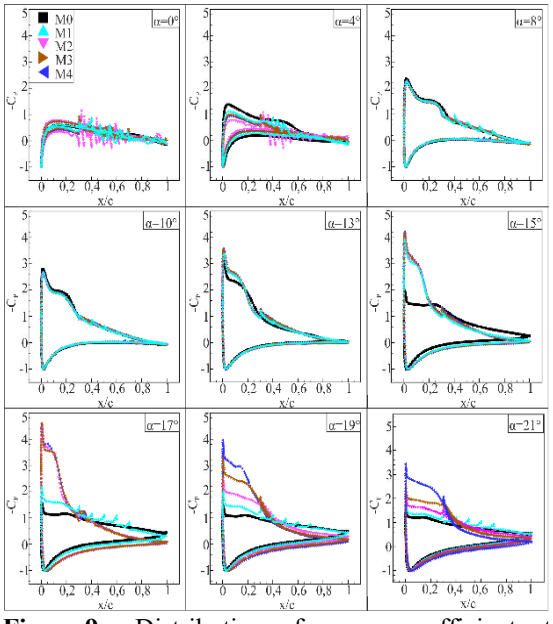

Figure 9. Distributions of pressure coefficients at various angles of attack

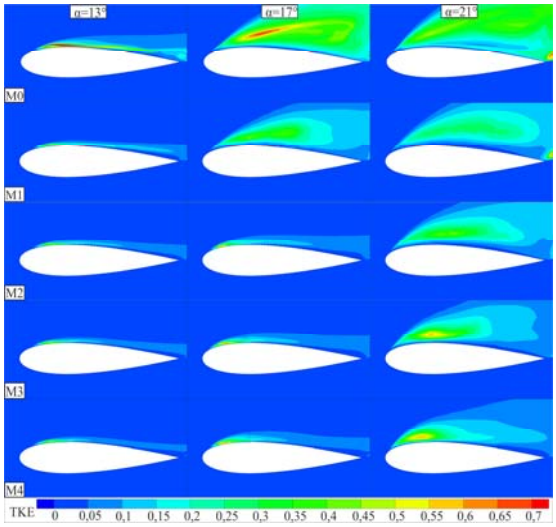

Figure 10. Turbulence Kinetic Energy (TKE) contours at angles of attack of α=13°, α=17° and α=21°

4. CONCLUSION

This study investigates the impact of riblet structures on the suction surface of a NACA 0018 airfoil on its aerodynamic performance through two-dimensional computational fluid dynamics (CFD) analysis at a Reynolds number of Re=1×10^5. The research parameters include riblet gap ratio and angle of attack, with comparative analysis against a plain model (airfoil without riblets).

Specifically, at α=13°, stall in the plain airfoil model, resulting from the merging of leading-edge separation and trailing edge separation, is prevented by riblet structures. The stall angle increases with decreasing gap ratio between the riblets, delaying stall by up to 6° compared to the clean airfoil model. Additionally, a substantial increase in the lift coefficient has been noted.

For s/c=0 riblet gap ratio, a notable up to 34% increase in the lift coefficient is observed compared to the plain airfoil model. When comparing lift-drag ratios (C_L/C_D) for the same models, this ratio experiences a remarkable 272% increase. Turbulence kinetic energy (TKE) values indicate lower turbulence intensity in controlled models, particularly starting from the leading edge.

Analysis of pressure coefficient distributions reveals that decreasing the distance between riblets until stall increases the pressure difference between the suction and pressure surfaces, thereby enhancing the lifting. Consequently, riblets, when employed as control elements, prove to be an effective flow control method for augmenting airfoil aerodynamic performance. The obtained data suggests an alternative approach applicable to studies on the maneuverability of small-scale unmanned aerial vehicles or efficiency improvements in wind turbines.

5. REFERENCES

1. Huber, A., Mueller, T., 1987. The Effect of Trip Wire Roughness on the Performance of the Wortmann FX 63-137 Airfoil at Low Reynolds Numbers. Experiments in Fluids, 5, 263-272.
2. Gopalarathnam, A., Broughton, B., McGranahan, B., Selig, M., 2001. Design of Low Reynolds Number Airfoils with Trips. Presented at the 19th AIAA Applied Aerodynamics Conference, Anaheim, CA, 2463.
3. Sareen, A., Deters, R.W., Henry, S.P., Selig, M.S., 2011. Drag Reduction Using Riblet Film Applied to Airfoils for Wind Turbines. Presented at the 49th AIAA Aerospace Sciences Meeting, Orlando, Florida, 558.
4. Lee, S.J., Lim, H.C., Han, M., Lee, S.S., 2005. Flow Control of Circular Cylinder with a V-Grooved Micro-Riblet Film. Fluid Dyn. Res., 37(4) , 246-266.
5. Vilkinis, P., Šereika, J., Pedišius, N., Zygmantas, G., 2022. Experimental Study of Flows over Triangular Riblets in Cavity-like Geometry. Experimental Thermal and Fluid Science 134, 110621.
6. Zhang, Y., Chen, H., Fu, S., Dong, W., 2018. Numerical Study of an Airfoil with Riblets Installed Based on Large Eddy Simulation. Aerospace Science and Technology 78, 661-670.
7. Akansu, Y.E., Özmert, M., Firat, E., 2011. Akış Kontrol Çubuğu ile Kare Kesitli Bir Küt Cisim Etrafındaki Akış Kontrolünde Hücum Açısının Girdap Kopma Olayına Etkisi. Isı Bilimi ve Tekniği Dergisi, 31(1), 109-120.

8. Timmer, W., 2008. Two-dimensional low-Reynolds Number Wind Tunnel Results for Airfoil NACA 0018. Wind Engineering, 32(6), 525-537.

9. Karasu, I., Genç, M.S., Açıkel, H.H., 2013. Numerical Study on Low Reynolds Number Flows Over an Aerofoil. Journal of Applied Mechanical Engineering, 2(5), 1000131.

10. Açıkel, H.H., Genç, M.S., 2018. Control of Laminar Separation Bubble over Wind Turbine Airfoil Using Partial Flexibility on Suction Surface. Energy 165, 176-190.

11. Güler, A., Seyhan, M., Akansu, Y., 2018. Effect of Signal Modulation of DBD Plasma Actuator on Flow Control around NACA 0015. Isı Bilimi ve Tekniği Dergisi, 38(1), 95-105.

12. Hussein, E., Azziz, H., Rashid, F., 2021. Aerodynamic Study of Slotted Flap for NACA 24012 Airfoil by Dynamic Mesh Techniques and Visualization Flow. Journal of Thermal Engineering, 7(2), 230-239.

13. Ozkan, G.M., Egitmen, H., 2022. Turbulent Structures in an Airfoil Wake at Ultra-low to Low Reynolds Numbers. Experimental Thermal and Fluid Science 134, 110622.

14. Lee, S.J., Jang, Y.G., 2005. Control of Flow Around a NACA 0012 Airfoil with a Micro-riblet Film. Journal of Fluids and Structures, 20(5), 659-672.

15. Wu, Z., Li, S., Liu, M., Wang, S., Yang, H., Liang, X., 2019. Numerical Research on the Turbulent Drag Reduction Mechanism of a Transverse Groove Structure on an Airfoil Blade. Engineering Applications of Computational Fluid Mechanics, 13(1), 1024-1035.

16. Tiainen, J., Grönman, A., Jaatinen-Värri, A., Pyy, L., 2020. Effect of Non-ideally Manufactured Riblets on Airfoil and Wind Turbine Performance. Renewable Energy 155, 79-89.

17. Yang, X., Wang, J., Jiang, B., Li, Z., Xiao, Q., 2021. Numerical Study of Effect of Sawtooth Riblets on Low-Reynolds-Number Airfoil Flow Characteristic and Aerodynamic Performance. Processes, 9(12), 2102.

18. Meena, M.G., Taira, K., Asai, K., 2018. Airfoil-Wake Modification with Gurney Flap at Low Reynolds Number. AIAA Journal, 56(4), 1348-1359.

19. Göv, İ., Doğru, M.H., Korkmaz, Ü., 2019. Uçuş Esnasında Değiştirilebilir Kanat Profili Kullanarak NACA 4412'nin Aerodinamik Performansının Artırılması. Gazi Üniversitesi Mühendislik-Mimarlık Fakültesi Dergisi 34(2), 1109-1125.

20. Harris, R.E., 2013. Adaptive Cartesian Immersed Boundary Method for Simulation of Flow over Flexible Geometries. AIAA Journal, 51(1), 53-69.

21. Tang, J., Viieru, D., Shyy, W., 2008. Effects of Reynolds Number and Flapping Kinematics on Hovering Aerodynamics. AIAA Journal, 46(4), 967-976.

22. Walters, D.K., Leylek, J.H., 2004. A New Model for Boundary Layer Transition Using a Single-point RANS Approach. J. Turbomach., 126(1), 193-202.

23. Walters, D.K., Cokljat, D., 2008. A Three-Equation Eddy-Viscosity Model for Reynolds-Averaged Navier–Stokes Simulations of Transitional Flow. Journal of Fluids Engineering, 130(12), 121401.

24. Aftab, S.M.A., Mohd Rafie, A.S., Razak, N.A., Ahmad, K.A., 2016. Turbulence Model Selection for Low Reynolds Number Flows. PLoS ONE, 11(4), e0153755.

25. Ahmed, Y.M., Elbatran, A.H., 2018. Numerical Study of the Flow Field Characteristics over a Backward Facing Step using k-kl-ω Turbulence Model: Comparison with Different Models. World Journal of Engineering, 15(1), 173-180.

26. Gaggero, S., Villa, D., 2018. Improving Model Scale Propeller Performance Prediction Using the k-k L-ω Transition Model in OpenFOAM. International Shipbuilding Progress, 65(2), 187-226.

27. Salimipour, E., 2019. A Modification of the k-k-ω Turbulence Model for Simulation of Short and Long Separation Bubbles. Computers & Fluids, 181, 67-76.